Fabrication of antibacterial mixed matrix nanocomposite membranes using hybrid nanostructure of silver coated multi-walled carbon nanotubes

Saif Al Aani, Virginia Gomez, Chris J. Wright, Nidal Hilal

PII: S1385-8947(17)30980-4
DOI: http://dx.doi.org/10.1016/j.cej.2017.06.029
Reference: CEJ 17110

To appear in: *Chemical Engineering Journal*

Received Date: 2 May 2017
Revised Date: 5 June 2017
Accepted Date: 6 June 2017

Please cite this article as: S. Al Aani, V. Gomez, C.J. Wright, N. Hilal, Fabrication of antibacterial mixed matrix nanocomposite membranes using hybrid nanostructure of silver coated multi-walled carbon nanotubes, *Chemical Engineering Journal* (2017), doi: http://dx.doi.org/10.1016/j.cej.2017.06.029

Fabrication of antibacterial mixed matrix nanocomposite membranes using hybrid nanostructure of silver coated multi-walled carbon nanotubes

Saif Al Aani[a], Virginia Gomez[b], Chris J. Wright[c], Nidal Hilal[a*]

[a] Centre for water Advanced Technologies and Environmental Research (CWATER), College of Engineering, Swansea University, Fabian Way, Swansea SA1 8EN, UK

[b] Energy Safety Research Institute (ESRI), College of Engineering, Swansea University, Fabian Way, Swansea SA1 8EN, UK

[c] Biomaterials, Biofouling and Biofilms Engineering Laboratory (B^3EL), The Systems and Process Engineering Centre (SPEC), College of Engineering, Swansea University, Fabian Way, Swansea SA1 8EN, UK

Abstract

The function of separation membranes can be significantly improved by the integration of nanoparticles that can improve not only the mechanical properties of the membrane but also reduce the propensity of the surface to foul. The research of the paper presents the development of a novel nanocomposite membrane incorporating antimicrobial nanoparticles which have the potential to lower membrane biofouling; a major problem in many industries that exploit membrane technology. Antibacterial hybrid nanostructures (HNS) comprising of multi-walled carbon nanotubes (MWCNTs) coated with silver nanoparticles (AgNPs) were successfully synthesized via a facile and rapid method using a microwave treatment. The HNS were incorporated into polyethersulfone (PES) ultrafiltration (UF) membranes via the classical phase inversion technique in order to assess their antimicrobial properties against two bacterial species; *E.coli* and *S.aureus*. Different techniques were used to characterize HNS powders and a number of loading weights of the HNS were blended with PES flakes to assess the resultant nanocomposite membranes. The nanocomposite membranes displayed an increase in their antibacterial activity against the two species with increasing the loading weight of HNS.

***Keywords*:** Antibacterial nanocomposite membranes, biofouling, silver nanoparticles, multi walled carbon nanotubes.

Corresponding author:
Email Address: n.hilal@swansea.ac.uk. (N. Hilal)

1 Introduction

As a new class of membranes, nanocomposite membranes are currently attracting a tremendous amount of research activity. These membranes that merge the beneficial properties of organic polymers and nanoscale materials are expected to revolutionize current membranes, and create innovative solutions in membrane technology through providing alternative strategies to control and mitigate membrane surface fouling; one of the key problems for the application of membranes.

Biological fouling is considered as the most inherently complex form of fouling. It is defined by microbial cell adhesion and subsequent colonization at the membrane surface forming microbial biofilm. Commonly, microbial colonization of the membrane surface is initialized by irreversible adhesion of one type of bacteria or more, followed by the growth and multiplication of the surface-bound cells in the presence of feed nutrients [1]. Once the microbes attach at the surface and form a matrix of extra-cellular polymers, their removal will extremely arduous even with the application of biocides [2]. Thus, biofouling represents the major concern for industries that exploit membrane technology including water, food and pharmaceuticals. As an alternative to disinfectant application, nanotechnology has impacted on the design and fabrication of nanocomposite membranes with the potential for creating self-cleaning and antimicrobial surfaces.

Within the wide range of commercially available nanoscale materials, silver nanoparticles (Ag-NPs) have gained special interest as unique antimicrobial additives in a broad range of applications. This is due to their unique antimicrobial properties alongside their electrical and optical characteristics [3, 4]. Even though their antimicrobial mechanisms are still under debate and not comprehensively understood [5, 6], their biocidal activity is well recognized as a highly desirable capability that they bestow on a membrane surface to resist biofouling and impart self-cleaning characteristics. On this basis, a large amount of work has been devoted for developing such nanocomposites membranes [7, 8]. As an important consideration when developing nanocomposite membranes for the control of biofouling, it is crucial to sustain antimicrobial activity and avoid the rapid depletion of nanosilver (nAg) that could diminish the antibacterial activity of nAg, and increase environmental issues and cost constraints. Attempts have been stepped forward to ameliorate

the interactions between these metallic nanoparticles and host polymeric chain to overcome these limitations. One of the most pragmatic approaches used for this target was through revising the surface characteristics of Ag-NPs via chemical treatment [9]. Various functional groups for modification/functionalization are available to increase their stability in the host polymer e.g., phosphoric acid, carboxylic acid, dopamine and silane coupling agents [10].

Apart from that, intensive researches are focusing on integration of one-dimensional nanoscale materials (1D-NMs) or two-dimensional (2D-NMs) with zero-dimensional (0D-NPs) into one hybrid nanostructure (HNS), which found their way in countless applications such as; fuel cells, photocatalysis, electrocatalysis, solar cells, sensors, supercapacitors, batteries and hydrogen storage applications. Applying these HNS could potentially exhibit not only the unique characteristics of 1D/2D and 0D at the nanoscale level, but also may possess novel chemical and physical properties as a result of the synergic effects of both nanomaterials that might not be obtainable to their individual component alone [11]. Several HNS targeting water and wastewater treatment have been reported in the recent few years [12, 13]. Parallel to this steadily evolution in HNS structures and applications. Functionalization of polymeric membrane aiming for a specific application has been evinced with these tailored nanostructures. For antibacterial nanocomposite membranes, Xu *et al.* blended AgNPs decorated Cu_2O nanowires (NWs) with PSF via phase inversion. To facilitate the deposition of AgNPs on the surface of Cu_2O, *L*-dopa has been grafted onto NWs surface by *in situ* polymerization to create zwitterionic surface. The nanocomposite membranes held remarkable antibacterial against *E. coli* and *S. aureus* with controlled release of Ag^+ [14]. Recently, Faria *et al.* conducted a research to functionalize TFC membranes with GO-Ag. Results referred to a promising inactivation rate against attached *P. aeruginosa* (up to 80%) without sacrificing the intrinsic transport properties for the modified membranes [15]. A number of HNS employed in fabrication malfunctional nanocomposite membranes have been reported in the literature for waste water treatment and desalination applications [16-19]. Another interesting 1D nanoscale carrier is carbon nanotubes (CNTs). Since its discovery in 1991, CNTs have turned into an established material in considerable commercial products [20]. Plentiful research endeavor has devoted on CNTs due to their tuneable thermal and electrical characteristics, high surface area to volume ratio, light weight, novel superlative strength and optical properties. Unsurprisingly, the assembly of carbon nanotubes (CNTs) along with the antibacterial Ag-NPs into one synergic HNS enticed tremendous applications, especially those targeting antimicrobial and self-cleaning surfaces. CNTs have been proven as a favorable templates for robustly tethering metallic NPs on their surfaces aiming for better

stabilization and dispersion of NPs [21, 22]. Utilization of CNTs as a carrier could hinder the aggregation and weak stability of unmodified AgNPs, and ultimately broadens their potential applications as unique antibacterial additives in nanocomposite membrane applications. Aside from this, it is worth mentioning that pristine nanotubes exhibit limited attractive interactions with metal/metal oxide, and thus unsurprisingly poor coating quality. Moreover during CNTs preparation the presence of metal catalytic particles and amorphous carbon, as impurities, could add additional burden to the intended application [23]. Therefore, purification and functionalization of CNTs could be established to negate the hydrophobic nature of CNTs and broaden their promising scope. For this reason, different linking groups e.g. $-NH_2$, $-SO_3H$, -COOH, -OH, or $–CONH_2$ could be introduced to CNTs surface to facilitate linking different metal clusters to the nanotubes surface.

There are a number of methods that have been developed for anchoring metallic NPs on the surface of CNTs, which include chemical reduction, pulsed laser ablation, microwave treatment, solar radiation, electrochemical deposition and *in situ* deposition on modified CNTs. Among these techniques, microwave treatment with its beneficial characteristics of energy rapid heating and decreased sintering temperatures, has broad application. Microwave energy can be used in chemical synthesis, processing of new materials, and in purification methods of carbon nanotubes [24, 25]. CNTs suffer a rapid temperature increase under microwave irradiation [25]. By using the rapid and local Joule heating of carbon nanomaterials under microwaves, metallic NPs can be created on the surface of the nanotubes, where the localized heat created on the surface of the carbon nanomaterials can be used to decompose different metallic precursors resulting in the immediate creation of metal and metal oxide particles [26].

In this work, we aim to shed the light onto developing a nanocomposite polymeric membrane using Ag-CNTs based HNS as antibacterial additives. A facile, rapid, scalable and cost-effective way was used to prepare the HNS. This was carried via direct precipitation and decomposing of silver metal salts solution on the surface of MWCNTs with the aid of microwave treatment. AgNPs are created in seconds and the amount of silver in the final products were easily tuned by changing the initial amount of silver nitrate, to compare between two Ag loading level to the CNTs, on the performance of the final HNS. After impregnating the prepared HNS into nanocomposite membranes, they were tested for evaluating their bacteriostatic properties against two pathogens. To the best of the authors' knowledge, no one, so far, has used microwave treatment in the preparation of HNS for nanocomposite membrane fabrication. Moreover, to assess and compare the influence of

varying Ag loading wt.% to CNTs on the morphological and antibacterial characteristics of nanocomposite membranes.

2 *Experimental*

2.1 Materials and reagents:

Raw MWCNTs, produced by chemical vapour deposition (CVD) method, were purchased from Chengdu Organic Chemicals Co. Ltd (China), Polyethersulfone (PES) flakes (M.wt 75,000) were kindly donated by BSAF Co. Ltd (Germany). Nitric acid (HNO_3) 69% wt/v, absolute Methanol and ethanol, Silver nitrate (AgN_3O_3, purity ≥99%), polyvinylpyrrolidone (PVP 40K), *N*-methyl-2-pyrrolidone (NMP) with ≥99% purity, polyethylene glycol PEG and polyethylene oxide PEO, Glutaraldehyde 50% v/v for fixation the bacteria, and all related chemicals and biological agents used for bacterial tests (e.g. Phosphate Buffer Solution (PBS), nutrient agar medium, Mueller Hinton Broth (MHB), and neutralizer) were purchased from Sigma-Aldrich (UK). Two bacterial species; *Escherichia coli* (ACIB 8277) and *Staphylococcus aureus* (ATCC 6538P) were provided from Microbiology laboratories-Swansea University.

2.2 Synthesis of hybrid nanostructured materials.

Herein, in order to eliminate the amorphous carbon, trace metal catalysts and to carboxylate the pristine MWCNTs (p-MWCNTs), 1000 mg of p-MWCNTs was dispersed in 200 ml HNO_3. The suspension was bath-sonicated for 15 minutes and then connected to a condenser for reflux under 120 ºC for 48 hrs. Later, the solution was left to cool at room temperature before diluting it with DI water. The resultant precursor was then filtered through a 0.22 µm cellulose nitrate membrane and washed with DI water until the pH had neutralized. Finally, the sample was dried overnight in a vacuum dryer at 40 ºC

For decorating the nanotubes, 10 and 20 loading wt.% of Ag to CNTs was used and the samples abbreviated as 10HNS and 20HNS respectively. A concentration of 1.17 mM and 2.35 mM silver nitrate in methanol were bath sonicated individually for 60 min to yield 10 and 20 wt. % silver on CNTs, respectively. Then, 127 mg of carboxylated MWCNTs, prepared earlier, was added to the solution and sonicated for another 30 min utilizing a horn sonicator (Vibra cell ™ – Sonics, USA). Thereafter, the precursor was dried at 35 ºC in a vacuum oven (vacumcenter, Salvis LAB- Switzerland). Finally, to physically deposit the Ag NP on the CNTs surface, the sample was treated by microwave heating for 10 min. A

domestic 1000 W microwave oven (Panasonic NN-CT579SBPQ) was used as the microwave source in all the experiments. In all microwave reactions, the sample was placed in a glass vial and microwaved at 1000 Watt power. Two Pyrex beakers 2/3 full of water were placed in the microwave to prevent overheating and replaced with cold water every one minute.

2.3 Membrane fabrication with HNS.

All nanocomposite membranes were prepared via the classical phase inversion technique. Two groups of modified membranes, using 10HNS and 20HNS were prepared. For each group, the amount of HNS added to the polymer (PES) was varied, see compositions in Table 1, to assess their influence on the overall performance of the nanocomposites in membrane fabrication and performance.

In the first instance, 2 wt.%. of PVP K30 (as pore former) was dissolved in NMP for an hour at 50 ºC, the solution was then cooled to room temperature before addition of HNS at the desired loading weight. Thereafter, the solution was sonicated for 30 minutes using a horn sonicator. PES flakes (16 wt.%) were gradually added to the precursor and vigorously mixed overnight. Degassing of the casting solution was carried out using a desiccator under vacuum condition for 1 hour. For solution casting, about 10 ml of casting solution was poured onto a glass substrate and casted with an automated casting knife (RK film applicator) at a regular shear rate (225 s^{-1}) with 200 µm clearance gap at ambient temperature. The resulting thin film was placed in a DI water bath at 20 ºC for precipitation. Within less than two minutes, the membrane detached from the glass plate indicating that the phase inversion was complete the membrane remained in the water bath for another 30 minutes. Finally, the membrane was washed with DI water and stored under water (DI) in a sealed container at 4 ºC, to be used in characterization. All membranes were cast at room temperature and relative humidity (RH% 45 ±5). Prior to testing, the membranes were inspected under light to make sure there were no pin holes, wrinkles or any defect that could make variation in their performance.

Table 1: Compositions of nanocomposite membranes using two concentrations of silver to nanotubes.

Nanocomposite membrane ID	Compositions				
	PES %	PVP %	NMP %	10HNS %	20HNS %
Control	16	2	82	0	0
0.05-10M	16	2	82	0.05	0
0.1-10M	16	2	82	0.1	0
0.3-10M	16	2	82	0.3	0

0.9-10M	16	2	82	0.9	0
0.05-20M	16	2	82	0	0.05
0.1-20M	16	2	82	0	0.1
0.3-20M	16	2	82	0	0.3
0.9-20M	16	2	82	0	0.9

2.4 Characterization of HNS and nanocomposite membranes

2.4.1 Characterization of HNS

A universal dip cell kit (ZEN1002) as an accessory for Zetasizer ZN nanoseries instrument (Malvern) was used to quantify the zeta potential (ζ) values of p-MWCNTs, functionalized carbon nanotubes (f-MWCNTs) ,10HNS and 20HNS. 5 mg of each sample was dispersed in 1L DI water and the pH was adjusted between pH3-pH11 to determine the isoelectric point. Fourier transform infrared spectrophotometry (FTIR) (PerkinsElmer) was used to confirm the presence of functional groups on the acid treated MWCNTs. X-Ray Diffraction Patterns (XRD) were recorded on a Brüker d8 DISCOVER diffractometer with a Cu kα X-Ray source (λ = 0.15418 nm) and analyzed using Match 2 software. Morphology for all samples were observed using a Scanning Electron Microscope (SEM) (Hitachi, S4800), at variant accelerating voltages and under high vacuum. While elemental composition analysis was achieved using Energy Dispersive X-ray Analysis (EDX) attached to the SEM. Thermal gravimetric analysis (TGA) (TA Instrument-Q600SDT) was used to study the thermal decomposition of HNS; about 5 mg of each sample was placed in an aluminium pan inside the combustion chamber and heated in presence of air up to 900 ºC (heating rate 10 ºC /min and air flow rate 100 ml/min). Raman spectra were recorded on Renishaw InVia confocal Raman microscope with 532 nm excitation laser. The potential antibacterial activity of HNS was demonstrated using Zone of Inhibition (ZOI) test. Two species of bacteria were used in this test; *Escherichia coli* (ACIB 8277) as a Gram-negative representative species and *Staphylococcus aureus* (ATCC 6538P) as a Gram- positive representative species. A single colony of each species taken from a nutrient agar Petri plate culture was used as an inoculum and cultured in 5 ml MHB and incubated at 37 ºC for 20 hours under shaking (40 rpm). Appropriate culture suspensions were then diluted to achieve a standard concentration of 0.5 McFarland determined at 600ODs, using a microplate reader (Synergy H1 hybrid, BMW Labtech, Germany). In the meantime, nutrient agar medium was prepared, sterilized in an autoclave at 121 ºC, then poured into sterile 90 mm plates and allowed to set at ambient temperature. Thereafter, 200 µl of bacterial cultures was pipetted on the surface of the agar,

spread using sterile cotton swap, and left for a 10-minute period for pre-incubation. Later, 3 mg of each sample (f-MWCNTs, 10HNS, 20HNS) was placed on the surface of the agar and incubated at 37 ºC for 24 hours. Finally, the plates were inspected for any inhibition zone of growth and the diameter of the zone measured.

2.4.2 Characterization of nanocomposite membranes.

2.4.2.1 Pure Water Flux (PWF)

PWF was computed using a cross-flow filtration rig and having an active membrane area of 12.6 cm^2. After compacting the nanocomposite coupons at a transmission pressure of 5 bar for approximately 30 min, the pressure was reduced to 4 bars and the permeate flux was recorded automatically every one minute using data collection software (WinWedge 3.0) interfaced with an electronic balance (Precisa, XB3200C, Switzerland). The automated software converted the permeate weight data received from the balance into a flux, and recorded the values on an excel spreadsheet for previously set membrane area and time intervals.

2.4.2.2 Solute transport method

Mean pore size and pore size distribution of all nanocomposite membranes were determined using solute transport mode as described elsewhere[27]. PEG/PEO as uncharged organic solute models with various molecular weights were used during all the experiments. The lowest molecular weight of solute was firstly introduced, then followed by higher molecular weight solutions. After compacting the membranes, an aqueous solution of PEG, as a feed, was passed through the individual membranes. While the feed concentration was maintained at a low value (200 ppm). Solution temperature and trans-membrane pressure were kept constant at 22∓0.5 ºC and 4 bar, respectively, throughout all the tests. A sample from the permeate side was taken after 10 ml had passed through the membrane. Both feed and permeate concentrations were analysed by a Total Organic Carbon analyzer (TOC-L, Shimadzu), whereas different PEG solutes separation percent were calculated via the following Equation:

$$\%\boldsymbol{R} = \mathbf{1} - \left(\frac{\boldsymbol{Cp}}{\boldsymbol{Cf}}\right) \text{ ... ...Eq. 1}$$

Respectively, *Cf* and *Cp* represent the solute concentration in feed and permeate solution.

Whereas, the probability density function has been used to describe the various pore size distribution curves [27], as follow:

$$\frac{df(d_p)}{d(d_p)} = \frac{1}{d_p \, ln\sigma_p \, (2\pi)^{\frac{1}{2}}} \; \exp\left(- \frac{(\ln d_p - \ln \mu_p)^2}{2(\ln \sigma_p)^2}\right) \quad \text{.....Eq. 2}$$

2.4.2.3 Contact angle measurement

Surface hydrophilicity of the nanocomposite membranes was evaluated by a sessile drop method using a VCAoptima contact angle instrument. 4 µl droplet of DI water was placed on flat membranes, and an image of the droplet was automatically captured to determine the contact angle measurement using VCA Optima XE software.

2.4.2.4 Zeta potential (ζ)

Tangential streaming potential measurements were determined using an Electrokinetic Analyzer (Anton-Paar GmbH, Austria). Zeta potential measurements of the nanocomposite membranes were determined using 10 mM electrolyte (NaCl) concentration and pH range (2.5 -10.5).

2.4.2.5 Bacteriostatic activities of nanocomposites

The potential antibacterial activities of nanocomposite membranes were determined using ISO 20743 test. Two representative microorganism samples, Gram negative (*E. coli*) and Gram positives (*S. aureus*) were applied for this purpose. A single colony of each stain, taken from an inoculum plate, was cultured in 5 ml MHB and incubated at 37 ºC for 20 hours under shaking (40 rpm). Appropriate culture suspensions were then diluted to achieve a standard concentration of (1.0 x10^6 CFU/ml) determined at 600OD. Meanwhile each nanocomposite sample was cut into 1.5x1.5 cm^2 pieces and sterilized in 70% EtOH, rinsed with sterile DI water and allowed to dry at ambient temperature and sterile conditions. The membranes were then kept in sterile Falcon tubes and 50 µL inoculum was spread over the sample surface using disposable loops and then incubated for 24-hour period at 37 ºC. As a standard step in the ISO test procedure, 5 ml neutralizer was added to the samples aiming to stop any potential growth of species after this stage through creating an environment free of nutrients. The suspension was then vortexed to allow the bacteria to detach from the membrane surface.

Thereafter, 1 ml of the bacterial suspension was taken to make a serial dilution (up to 8 dilutions) using PBS at ratio 1/9 (suspension/diluent) for each dilution. 4-6 droplet (20 µL each) were then cultured on nutrient agar plates prior to incubation at 37 ºC for 24-hour. Finally, a colony plate counting method was used to count only the viable discrete colonies on the plate. In this established procedure, valid counts should only consider a certain number of colonies for each drop; minimum 2 to a maximum of 20. Any count not within this range was attributed to invalid results. This method has been widely applied in the literature and considered as a reliable, fast and precise way of determining microbial cell viability at surfaces [28]. To assess the antibacterial activity of the nanocomposites, the number of CFU/ml obtained after exposing the membranes to the bacterial cultures was determined and results were expressed in Log kill (Log of reduction factor calculated from dividing of CFU/ml obtained from nanocomposites to that obtained from the control membrane).

2.4.2.6 SEM imaging

The disruption of cell integrity of both microbial species induced by HNS was imaged by SEM. Membrane samples and inoculums ($1.0x10^6$ CFU/ml) were prepared and cultured as reported in the ISO test. For fixation of the bacteria on membrane surfaces, all samples were immersed in 4 ml glutaraldehyde (3% v/v) and placed in a fridge overnight at 4 ºC. Later, samples were rinsed with PBS twice before the dehydration process. Dehydration was carried out using sequential concentrations (25%, 50%, 75% and 100%) of ethanol (15 min each). Finally, before SEM imaging samples were coated with chromium by sputter coating (Quorum, Q150T ES, UK).

3 Results and discussion

3.1 HNS characterization

3.1.1 FTIR Spectra evaluation of MWCNTs

Applying concentrated HNO_3 for p-MWCNT purification has enhanced both purity and partial oxidation of nanotubes where number of functional groups, mainly carboxyl and hydroxyl, appeared after the acid treatment. Total Reflection Infrared spectra (FTIR) of p-MWNT and f-MWNTs from 700 to 4000 cm^{-1} is shown in (Fig. 1). The broad well defined peaks around 3376-3983 cm^{-1} can be ascribed to the stretching mode of a hydroxyl (-OH) bond [29]. Notable peaks were observed around 2903-2986 cm^{-1} that correspond to C-H symmetric and asymmetric stretching vibration, which is responsible for the stability of

nanotubes suspensions in aqueous phase [30, 31]. IR regions around 1650 cm^{-1} are assigned to oscillation of carboxyl (-COOH) groups, while the broad weak peak observed at 1399 cm^{-1} is probably associated with O-H bending deformation of -COOH acid groups [32]. The well-defined peak at 1064 cm^{-1} was correlated to the C-O stretch vibration. Thus, FTIR has confirmed the presence of oxygen/acid functional groups induced after acid treatment.

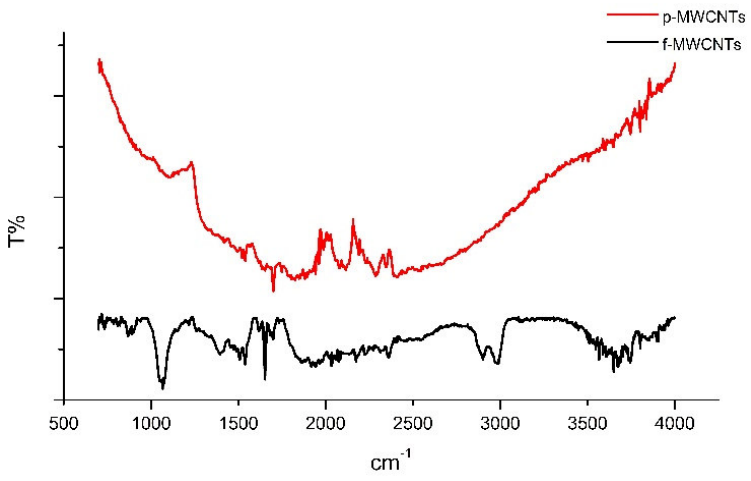

Figure 1 Fourier transform infrared spectroscopy (FT-IR) spectrum of p-MMWCNTs and f-MWCNTs.

3.1.2 Zeta potential measurements.

Zeta potential measurements were carried out as a function of pH (3-11) to quantify the degree of functionalization for f-MWCNTs, and to evaluate the role of depositing different loading levels of Ag NPs on the surface of f-MWCNTs (Fig. 2). It can be clearly seen that carboxylating the pristine nanotubes greatly influenced the zeta potential values. The isoelectric point of p-MWCNTs located at pH 4 has disappeared after functionalization where the plot shifted to more negative values even within a very high acidic environment. As confirmed in section (3.1.1), the presence of novel functional groups has given rise to higher negatively charged nanotubes. Indeed, this enhancement in the value of zeta potential (e.g. -27 to -43 at pH6) is expected to induce a better stability and dispersibility for nanotubes in the polymeric matrix [33], and also act as nucleation sites for later deposition of Ag on the surface of nanotubes [23]. However, Ag NPs deposition on the nanotubes had lowered zeta potential values for both 10HNS and 20HNS. This can be ascribed to the positively charged Ag NPs contribution to the total charge of the nanostructures [34]. This contribution was

higher in the case of 10HNS compared to that of 20HNS and was due to the higher surface to volume ratio of Ag in the 10HNS sample, as will be demonstrated in the next sections. Even though both hybrid nanostructures exhibited lower zeta values than f-MWCNTs, they are still higher than those of p-MWCNTs.

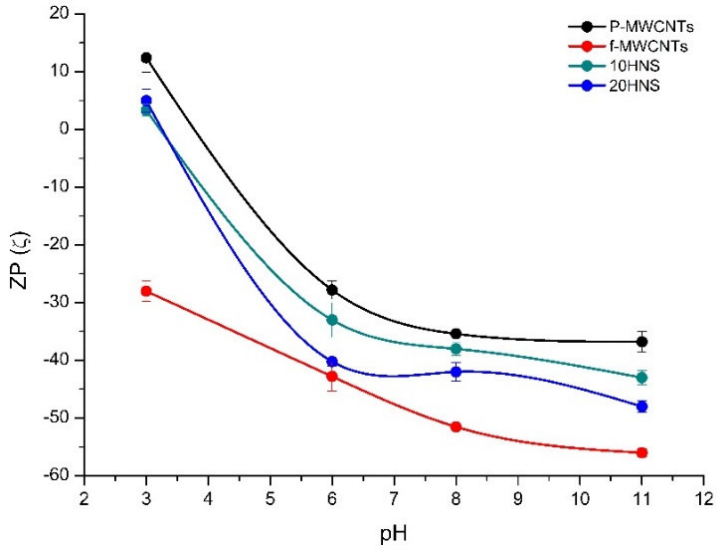

Figure 2: Zeta potential measurements as a function of pH for**;** raw, carboxilated and silver decorated nanotubes.

3.1.3 X-Ray Diffraction analysis

XRD diffraction patterns of the different carbon nanotube samples are shown in (Fig. 3). The carbon nanotubes, both pristine and functionalized, showed two diffraction peaks at 26 and 43° that correspond to the (002) and (100) reflections of the graphite layers' structure (COD 1200017 and COD 9011577) [16]. It's clear that amorphous carbon component, observed in the p-MWCNTs sample (the broad medium peak 27-35^{o}), has been removed after the acid treatment. Decorating carbon nanotubes with silver nanoparticles caused another three peaks at 38, 44 and 64° that correspond to the (111), (200) and (220) reflections related with the Ag (0) (COD 9011607). Interestingly, the peak (002) assigned to CNTs characteristics displayed lower intensity than pristine and functionalized nanotubes after decoration with Ag, where this reduction could be attributed to defects created on the surface of nanotubes during the decorating process [35]. Nevertheless, the XRD diffraction peaks of 10HNS are slightly widened due to the deposition of smaller metallic Ag-NPs existing as silver nanocrystal.

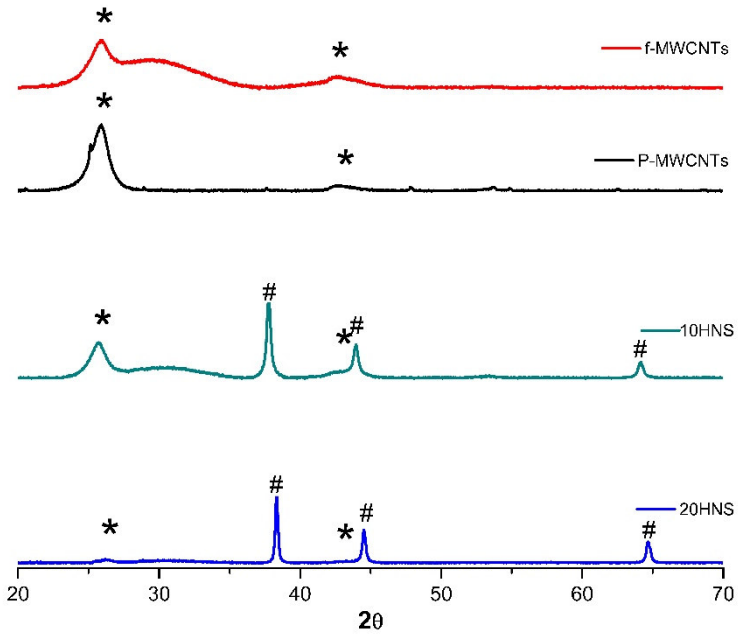

Figure 3: XRD patterns for; carboxilated, raw and silver decorated nanotubes. Main diffraction lines for graphite (*) and silver (#) phases are indicated.

3.1.4 Microscopic observation

Surface morphology of MWCNTs, prior and after silver decoration, were observed by SEM as shown in (Fig. 4). No apparent destruction was found in the structure of MWCNTs after treatment with concentrated HNO_3. (Fig. 4A and Fig. 4B) show a clear cylindrical nanostructure as the bundles aligned together through the action of van der Waals forces. The only difference between those two samples was their purity as confirmed by elemental analysis (EDX), (Fig. 5A and Fig. 5B). The residue of metallic catalysts residue was much less apparent in the f-MWCNTs sample than in the pristine one, indicating a higher degree of purity was achieved. (Fig. 4C and Fig. 4D) show the morphology of 10HNS and 20HNS respectively. As can be seen, it was difficult to observe Ag NPs deposition on the surface of nanotubes by SEM imaging. Possibly, this could be due to the small particle sizes of AgNPs on the surface of CNTs in the 10HNS sample. However, homogenous distribution, without distinctive aggregation, was observed in the 20HNS sample due to the higher loading wt. % of Ag used in preparation. This observation of larger Ag-NPs could be due to the limited number of active anchoring sites (e.g. defects) on the surface of CNTs. Indeed, the active sites were oversaturated with the higher Ag content in the 20HNS. Consequently, the remaining decomposed silver continued deposition onto the previously anchored seeds to

form larger size AgNPs [26]. The presence of Ag was confirmed by Ag spectra detected for both decorated samples at 3 keV, (Fig. 5C and Fig. 5D). Finally, the results agreed with those obtained from both TGA (section 3.1.5) and theoretical calculation in terms of compositions (section 2.2).

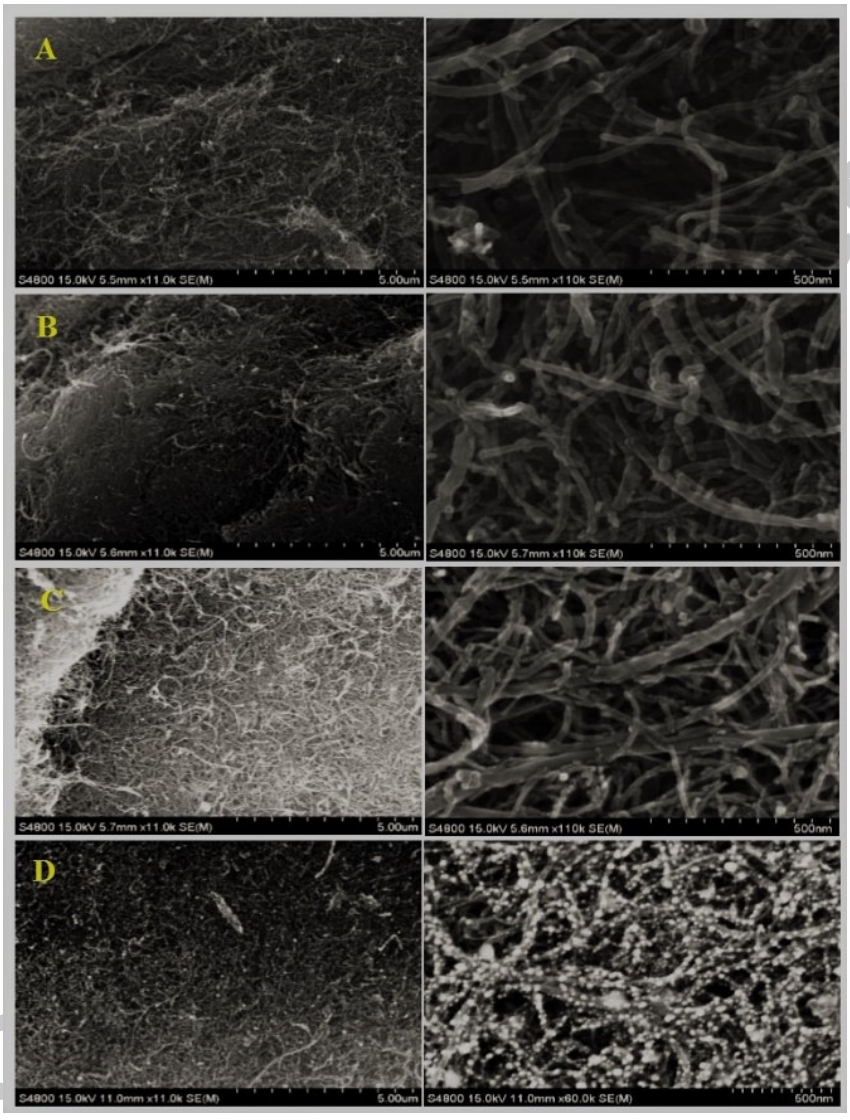

Figure 4: 5 µm (Left) and 500 nm (Right) SEM images for (A) p-MWCNTs, (B) f-MWCNTs, (C) 10HNS, and (D) 20HNS modulated by microwave irradiation.

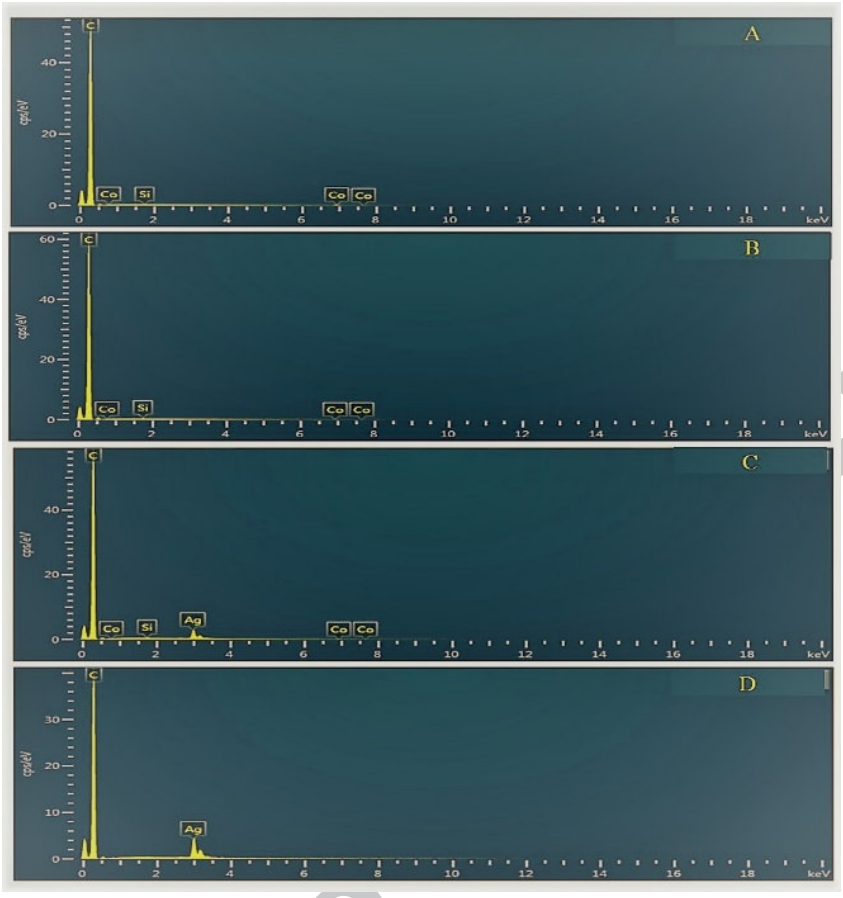

Figure 5: Elemental composition of (A) p-MWCNTs, (B) f-MWCNTs, (C) 10HNS, and (D) 20HNS modulated by microwave irradiation.

3.1.5 Thermal behavior Analysis

The initial, main and char decomposition regions of TGA curves are illustrated in (Fig. 6). The slight initial weight loses detected below the onset decomposition temperature of samples are ascribed to the ambient moisture content in the samples or evolution of functional groups [30]. In fact, the significant change in the thermal properties and weight loses under an oxidative environment was different for each sample. A gradual slight weight loss (9.2%) was noticed for f-MWCNTs before the significant loss at 551 ºC. This could be linked to the decomposition of the thermally unstable organic functional moieties in the functionalized sample [36]. Compared to f-MWCNTs, p-MWCNTs were distinctly more stable and only 2.2% weight loss was detected with a lower decomposition start temperature (467 ºC), which could be attributed to the variation in the metal catalyst residues and graphitization degree before and after acid treatment [37]. The presence of metal catalyst

residues was decreased after acid treatment, from 2.3 wt.% to 0.3 wt.%, indicating further purification was accomplished. Interestingly, Ag deposition on the nanotubes' side walls significantly reduced the onset decomposition temperature for both 10HNS and 20HNS to 309 ºC and 266 ºC, respectively. Ag is known as functional oxidative catalyst able to catalyze the low temperature oxidation of nanotubes under O_2 atmosphere [34]. Amount of Ag, after decomposition of 10HNS and 20 HNS, has confirmed the theoretical loading level used in this work and was found to be 10.5% and 20.2 %., respectively.

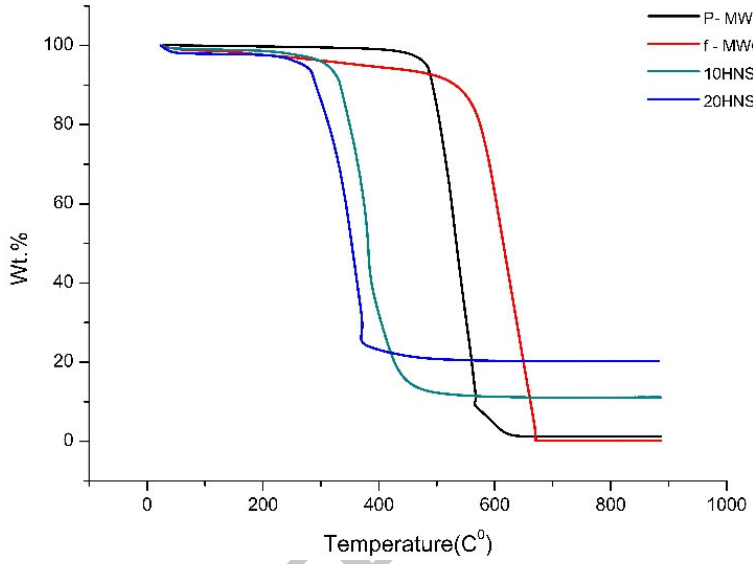

Figure 6:Thermogravimetric curves of p-MWCNT, f-MWCNTs, 10HNS and 20HNS.

3.1.6 Raman spectroscopy

The structural changes, prior and after functionalization along with decorated MWCNTs, were determined by Raman spectroscopy bands, (Fig. 7) (Left). All carbon peaks contributing to Raman spectra lie within 1000-1700 cm^{-1}. The characteristic feature of all sp^2 hybridized carbon allotropes was confirmed by the appearance of a band (G-band) at 1572 cm^{-1} [38]. While the other additional band (D-band) at 1340 cm^{-1} identifies the defects/disorders in the sp^2 hybridized carbon, which could be impurities, lattice distortions in the nanotubes, sp^3 hybridized bonds, and/or existing functional groups created after acid treatment. While the mode at 2685 cm^{-1} was attributed to the first overtone of the band at D and is denoted as G' mode [39]. The intensity ratio of G-band and D-band (I_G/I_D) has been used to identify and monitor the presupposed defects on the MWCNTs after processing with HNO_3 and further

decoration with Ag. This (I_G/I_D) was found to be 0.76, 0.85, 0.89 for p-MWCNTs, f-MWCNTs and 10HNS, respectively. The changes in the intensities of the bands and (I_G/I_D) evidenced an increase in the defects and disorder in the MWCNTs after acid treatment. In addition, further changes were also found to be induced into Raman scatter intensity after silver deposition, which is a substantiation for Ag-NPs attachment. Furthermore, a more defined peak on the right side of the G-band was evolved around 1620 cm^{-1} (D'-band) after p-MWCNTs processing, Figure 7: Raman spectroscopy results for pristine, functionalized and Ag decorated MWCNTs, 1000-3000 cm^{-1} (Left), and 1500-1700 cm^{-1} (Right).(Fig. 7) (Right). This evolution of the peak was ascribed to functionalization and later on to deposition of Ag

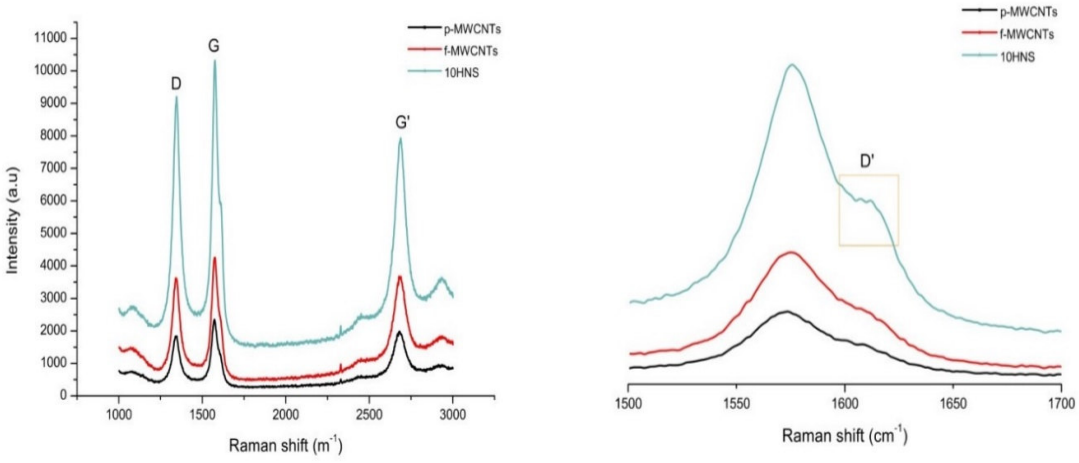

on the surface of nanotubes [40]. Herein, it should be noted that AgNPs could preferentially grow on the surface defects of nanotubes, which explain the small overall increase in I_G/I_D after decorating the MWCNTs [26, 41].

Figure 7: Raman spectroscopy results for pristine, functionalized and Ag decorated MWCNTs, 1000-3000 cm^{-1} (Left), and 1500-1700 cm^{-1} (Right).

3.1.7 Zone of inhibition.

The variation in the zone of inhibition (ZOI) caused by samples of the nanoparticles can be observed in (Figure 8). Both 10HNS and 20HNS have manifested bacteriostatic capabilities against both *E. coli* and *S. aureus*. The ZOI is shown by the clear ring surrounding the sample, which resulted from the prevention of microbial growth. Meanwhile, there was no observable inhibition with the f-MWCNTs as shown in (Figure 8A). 10HNS had higher antibacterial activity against both species compared to that of the 20HNS sample. ZOI

diameter was found to be 19.7 mm and 15.2 mm for 10HNS against *E. coli* and S. aureus, respectively (Fig. 8B). While ZOI diameter decreased to 12.5 mm and 10.9 mm, against *E. coli* and *S. aureus* respectively, when using 20HNS at the same inoculum concentration ($1.5x10^8$ CFU ml^{-1}), (Fig. 8C). The higher inhibition of nanostructures towards *E. coli* as compared to that of *S. aureus* was thought to be due to the variance in cell wall structure, the difference in the thickness of peptidoglycan layer between Gram negative and Gram positive bacteria. A thicker peptidoglycan layer of the cell wall is associated with the Gram positive *S. aureus* (20-80 nm) compared to the Gram negative *E. coli* (7-8 nm) [42]. The different activity of the silver ions against the different bacterial types may also be due to differences in the charge nature of the different cell walls of Gram positive and Gram negative bacteria; the electrostatic attraction between positively charged Ag and the negatively charged cell walls may be different [5], leading to different degrees of hindrance as the silver ions approach the microbial cells.

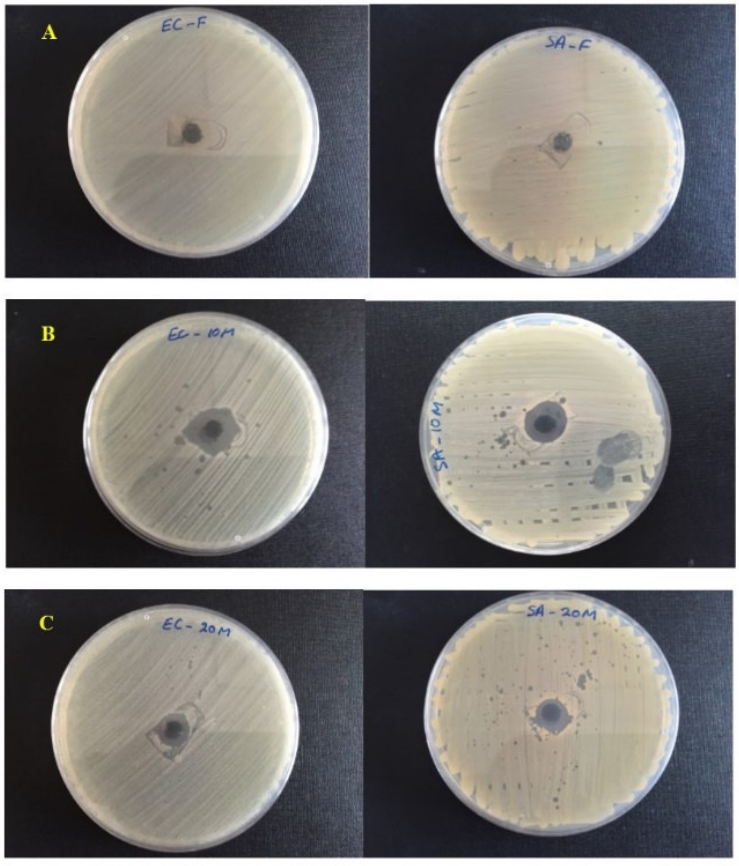

Figure 8: Inhibition zone against *EC* (Left) and *SA* (Right) for (A) f-MWCNTs, (B) 10HNS and (C) 20HNS.

3.2 Nanocomposite membranes

To establish a deeper insight into the amelioration of membrane materials when they are fabricated by doping with HNS to produce nanocomposite membranes Table. 1, an extensive characterization of the membrane parameters that influence membrane performance was undertaken. Thus, nanocomposite membranes were characterized in terms of PWF, pore size and pore size distribution, hydrophilicity, surface zeta potential measurements and surface morphology. Moreover, bacteriostatic activity of these nanocomposites was also tested to confirm the efficacy of the active materials after membrane fabrication and to identify the influence of loading wt.% of HNS and Ag loading level to MWCNTs on the prepared nanocomposites. It should be noted that increasing the concentration of both 10HNS or 20HNS in the casting solution resulted in darker nanocomposites; the undersides of the membranes were significantly lighter in colour than the top surface for all nanocomposites, (Fig. 9). This was due to the migration and concentration of the HNS at the top surface during the phase inversion process.

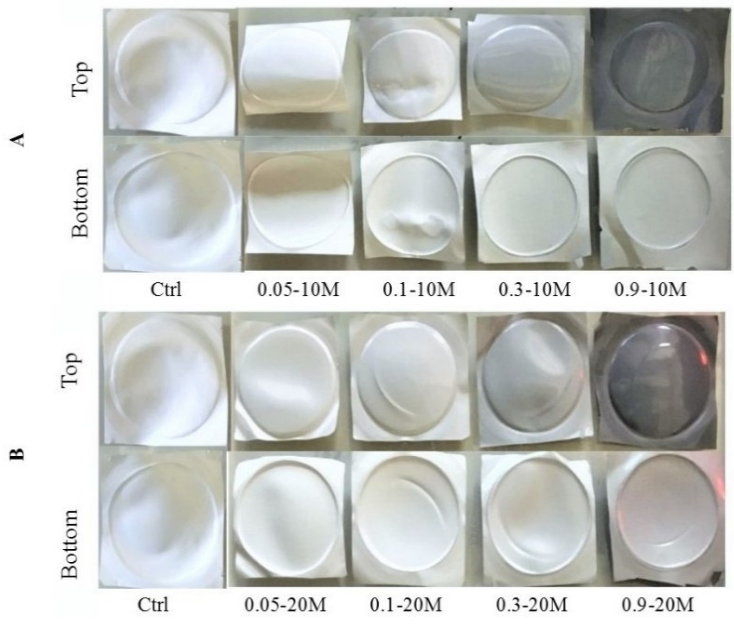

Figure 9: Top and bottom surface of (A) nanocomposites prepared with 10HNS and (B) nanocomposites prepared with 20HNS.

3.2.1 Cross section morphology of nanocomposites

Cross sectional study was conducted by SEM to qualitatively assess the cross-section morphology of the nanocomposite membranes, since structure has a significant influence on membranes transport mechanisms. All cross-sectional images obtained from bare and nanocomposite membranes demonstrate a typical asymmetric structure, (Fig. 10). A clear dense active and porous supporting layer can be observed for all the membranes. Control PES membrane had a well-developed skin layer supported by wide finger-like macro-pores at the bottom of the membrane, (Fig. 10A). This structure was formed due to the low polymer dope solution used to prepare the membrane. The structure is favored as at low viscous casting solutions the nonsolvent exchange rate into the polymer lean phase exceeds the outward solvent diffusion rate [43]. Incorporating a small amount of the HNS into the PES matrix (up to 0.1%) promoted the formation of big macrovoids in the sub layer, (Fig. 10B and Fig. 10C). While further increase in HNS content suppressed the formation of these macrovoids, and led to narrower micro-pores with a finger-like shape oriented from the top to the bottom layer of the nanocomposites, this is a different shape to the micro-pores of the PES membrane, as seen in (Fig. 10D and Fig. 10E). This was due to the enhanced viscosity of the casting solution that hinders the solvent-nonsolvent exchange rate at the interface between the surface and the nonsolvent, producing a slightly denser skin layer and less porous membranes [44]. On the other hand, the 0.9-20M and 0.9-10M membranes had similar cross-sectional morphology, indicating no significant variation in their permeation characteristics would result from variation of the silver level in the HNS (Fig. 10F).

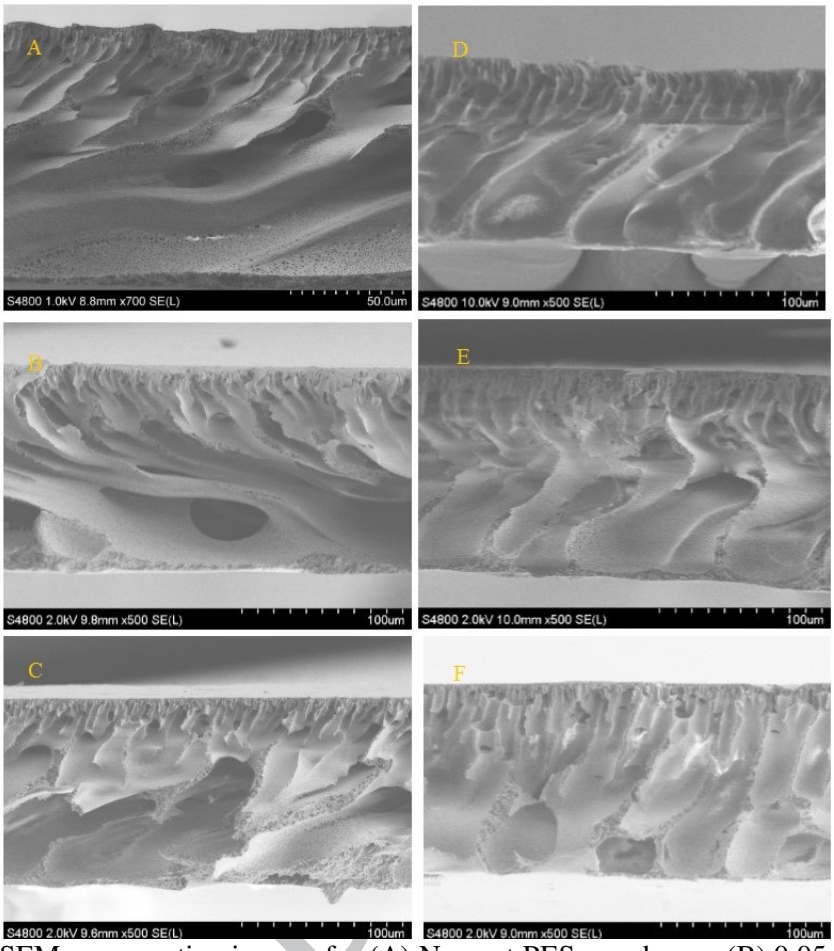

Figure 10 SEM cross section images for (A) Nascent PES membrane, (B) 0.05-10M, (C) 0.1-10M, (D) 0.3-10M, (E) 0.9-10M (F) 0.9-20M.

3.2.2 Static contact angle and hydrophilicity measurements

Contact angle measurement is a well-known technique for characterizing surface hydrophilicity/hydrophobicity, which informs analysis of membrane performance. A more hydrophilic membrane surface will result in a lower contact angle [45]. However, measurement of contact angle to express the hydrophilicity of a membrane material is not necessary conclusive, since several factors may impact on the hydrophilicity values such as porosity, roughness, pore size and pore size distribution [46]. As shown in (Fig. 11), the surface hydrophilicity/hydrophobicity of all nanocomposite membranes were lower compared to the nascent PES membrane. A noticeable gradual decrease in contact angle value was associated with each incremental increase in the concentration of HNS in the nanocomposites. This amelioration in hydrophilicity is believed to be induced by the

spontaneous migration and concentration of the well-dispersed hydrophilic HNS close to the top surface/water interface to reduce the interfacial energy during the phase inversion. This phenomena imparted more hydrophilicity to the hybrid nanocomposites [19]. These results are in contradiction with those conducted previously and revealed irregular positioning of nanotubes within the structure of nanocomposites, at higher loading than 0.4 wt.% [47]. Both sets of nanocomposite membranes, supplemented with 10HNS and 20HNS, had a comparable contact angle value (slightly higher hydrophilicity for 10HNS nanocomposites) when an identical concentration of the HNS was used. This suggests that the Ag loading level to the MWCNTs had little influence on the contact angle measurement of the nanocomposite membrane.

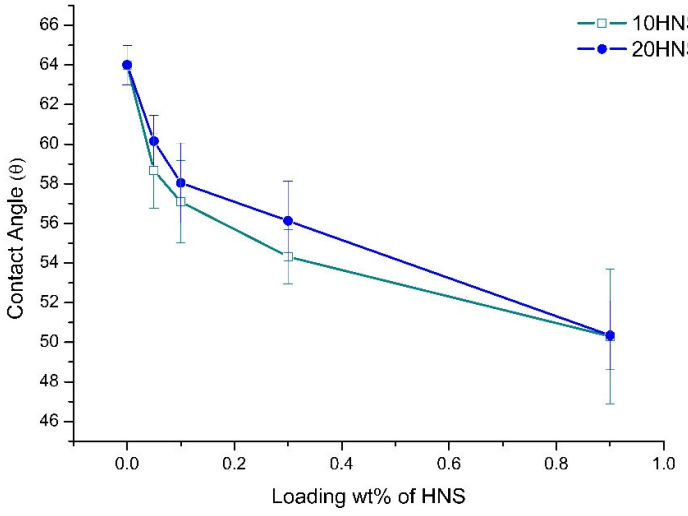

Figure 11: Contact angle measurements of nanocomposite membranes prepared with different loading weights of 10HNS and 20HNS

3.2.3 Mean pore size and pore size distribution determination

A solute transport model, as a standardized method, has been applied to determine the nanocomposite membranes geometric mean pore size (μ_p), geometric standard deviation (σ_p) around the mean pore size, and their distribution characteristics. This method relies on the correlation between solutes retention and their molecular size using uncharged solutes PEG/PEO with known molecular weights [27]. The μ_p and σ_p of the unmodified (control) and nanocomposites membranes are summarized in Table. 2. Addition of 10HNS to the control membrane did not dramatically change the surface pore size characteristics, at all loading

compositions. This indicates a very high degree of 10HNS dispersion inside the PES matrix. Indeed, negligible variation in the nanocomposites selectivity was obtained. Mean pore diameter of membranes were found to slightly increase from 10.93 nm to 11.69 nm with only 0.05% 10HNS. Further increase in the 10HNS composition, to 0.1 and 0.3%, led to a gradual decrease in the pore size. This decrease reached its minimum value at 0.9% with a pore diameter of 10.4 nm. It was expected that a very high loading (0.9%) would induce pore size narrowing due to the higher casting solution viscosity, which resulted from adding this amount of HNS. Geometric standard deviation values were comparable and reasonable for all UF membranes. Values of σ_p associated with their corresponding μ_p values ranged from 1.27-1.44. This indicates that all unmodified and nanocomposites were similar in their microstructure. On the other hand, incorporation of 20HNS into the polymeric matrix showed slightly higher $\mu_{p.}$ and σ_p values to those obtained from nanocomposites prepared using 10HNS.

Table 2: Geometric mean pore size and standard deviation of nanocomposite membranes.

Membrane ID	**Mean pore diameter (μ_p) (nm)**	**Geometric standard Deviation (σ_p)**
Control	10.93	1.37
0.05-10M	11.69	1.28
0.1-10M	11.15	1.34
0.3-10M	11.1	1.38
0.9-10M	10.4	1.40
0.05-20M	12.9	1.27
0.1-20M	12.3	1.29
0.3-20M	10.65	1.44
0.9-20M	10.57	1.40

The cumulative pore size distributions of the nanocomposites are presented in (Fig. 12). This provides further evidence that there was negligible difference in pore size distributions for all PES membrane. HNS addition, up to 0.3%, caused a slight shift to the right for the pore size cumulative curves. At 0.3% HNS, the curve was almost identical to the control PES membrane, which exhibited similar mean pore size and standard deviation. While only 0.9-10HNS nanocomposite curve shifted to the left. This behavior of the pore size distribution

curves suggests no appreciable agglomeration of the HNS within the polymer matrix occurred even at high HNS content.

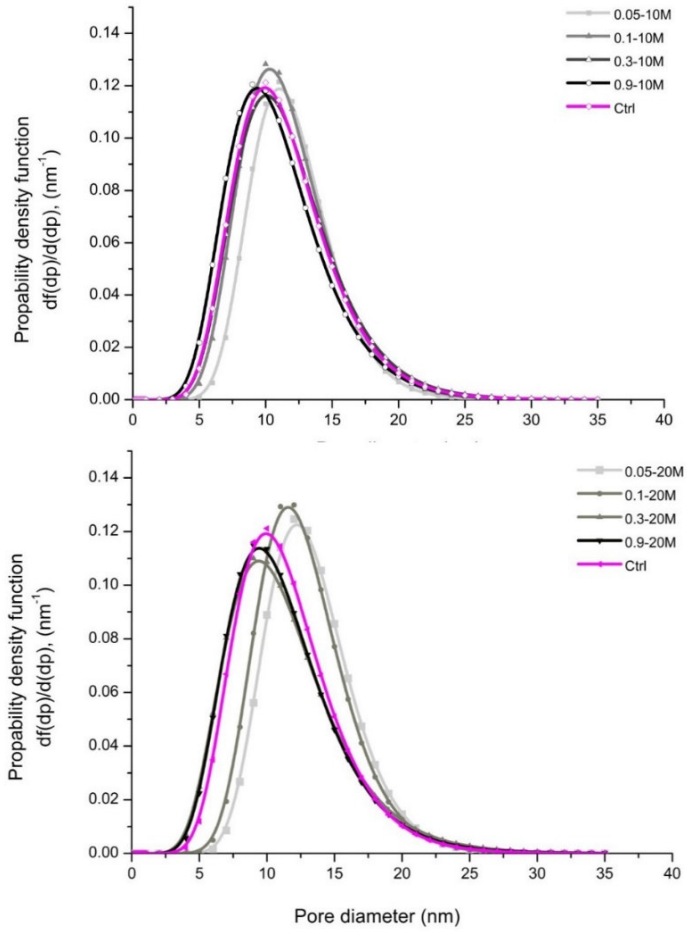

Figure 12: Pore size cumulative curves of nanocomposite membranes for 10HNS (Top) and 20HNS (Bottom).

3.2.4 Surface zeta potential of nanocomposite membranes

Surface zeta potential (ζ) of the membranes was characterized using a streaming potential technique. Zeta potential measurements are indispensable for fundamental insights into the separation mechanisms, membrane aging, membrane fouling and cleaning [48]. All modified and unmodified membranes were found to be negatively charged from pH 2.5 to pH 10.5, no isoelectric points could be identified, (Fig. 13). Results obtained for the nascent PES membrane were in agreement with previous research [49]. Incorporating the HNS within the polymeric matrix was seen to have palpable influence on the membrane, depending on the HNS concentration added. To the best of the authors' knowledge, there has been no research

examining the influence of loading weight, for any metal-carbon based HNS to a polymeric membrane, on surface zeta potential. Nanocomposite membranes with the lowest concentration of HNS exhibited the highest negative zeta potential values compared to others. Increasing the HNS loading to the PES not only lowered the negative zeta potential value of nanocomposites, but also narrowed the range of zeta potential measurements over the entire pH range studied. This upward trend was attributed to the positively charged Ag-NPs in the HNS. Higher amounts of HNS in the nanocomposite membrane gave rise to higher amounts of Ag^{+} to outweigh their counterpart negatively charged MWCNTs.

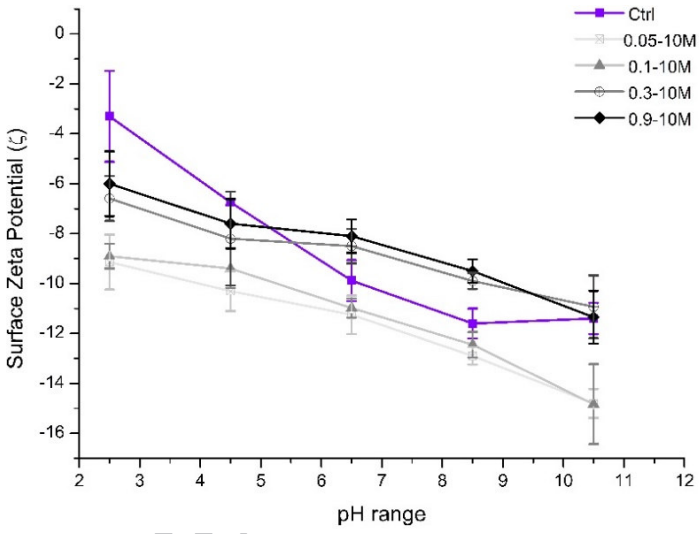

Figure 13: Surface Zeta potential of nascent and nanocomposites membranes at different loading weight of 10HNS.

3.2.5 Pure water flux

The Pure water flux (PWF) of the nanocomposites incorporating10HNS and 20HNS are presented in (Fig. 14), All nanocomposite membranes had improved PWF behavior as HNS content increased. Compared with unmodified PES membrane, the 10HNS concentration in the nanocomposite, from 0 to 0.05, 0.1, 0.3 and 0.9%, raised the PWF from 554 ($L.m^{-2}.h^{-1}$) to 693, 722, 746 and 556 ($L.m^{-2}.h^{-1}$), respectively. Interestingly, even though the 0.9-10HNS nanocomposite returned to a lower PWF, it was still comparable to that of unmodified PES membrane. Herein, the PWF data can explain the inter-correlation between the permeation characteristics of membranes and other characteristics such as hydrophilicity and solution casting viscosity. For instance, hydrophilicity data obtained have been agreed with PWF measurements for all nanocomposites, except 0.9-10HNS which had the lowest contact angle

but lower flux than other nanocomposites, as illustrated in (Fig. 11). The reduction in the flux may be attributed to the higher viscosity at 0.9% HNS concentration level that resulted in a slightly lower mean pore size and less porous structure, regardless of the lowest contact angle reported for this nanocomposite. This has been illustrated in the cross-section images earlier (section 3.2.1). To emphasize the role of hydrophilicity on the PWF of nanocomposite membranes, the 0.3-10HNS nanocomposite membranes had less porous structure than unmodified PES, a similar µp, but their PWF were significantly different. So far, the hydrophilicity effect can be considered as the dominant factor when the viscosity role is equimolar or low enough to discard it. On the other hand, nanocomposite membranes prepared using 20HNS displayed a similar trend but with higher PWF than membranes prepared with 10HNS. This may be due to the higher pore size obtained, since the

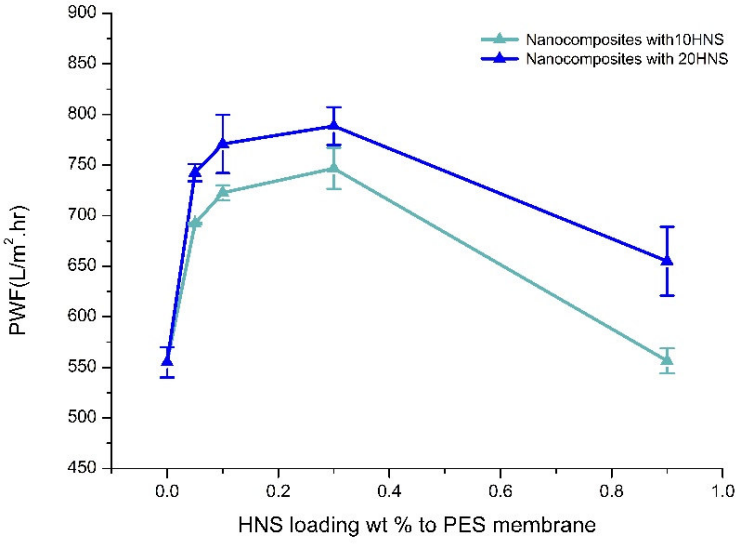

hydrophilicities of different membrane groups were almost identical.

Figure 14: Pure water flux behaviour of nanocomposite membranes prepared with 10HNS and 20HNS at different loading wt.%

3.2.6 Potential bacteriostatic activities of nanocomposites and Morphological characterization of microorganisms

It is well established that a successful antimicrobial surface could be identified by either direct kill of microbial cells, attachment inhibition of microbes or degradation of the extracellular polymeric substances (EPS) deposited during the biofilm formation [50]. Thus, the potential antibacterial activities of the nanocomposite membranes were measured and

expressed by Log kill as shown in (Fig. 15). Two microorganisms Gram negative *E. coli* and Gram positive *S. aureus*), as a model bacterial species were used along with a standard testing protocol (ISO 20743) for membranous material, No apparent kill was anticipated with unmodified PES membrane against both species. As expected the viability of bacteria decreased with increasing HNS concentration in the nanocomposites. This biocidal property of the nanocomposites reached its maximum capability at 0.9% 10HNS concentration with 4.24 and 2.9 Log kill against *E. coli* and *S. aureus*, respectively., *E. coli* was more sensitive to Ag than *S. aureus*. This difference in susceptibility is argued to be due to the cell wall thickness, with the cell wall of Gram positive bacteria being thicker than that of Gram negative bacteria [18]. The influence of nanobiocide size on the antibacterial activity of the nanocomposites cannot be disregarded. The smaller AgNPs found in nanocomposites prepared with 10HNS had higher activity than those prepared with 20HNS, where Log kill values were 3.8 for 0.9-20M compared to 4.24 for 0.9-10M nanocomposites. This could be due to the higher surface to volume ratio of silver in the 10HNS, which can display higher interactions with microorganisms and with silver supporting nanotubes.

Surface morphology of both membranes and cells were examined using SEM, (Fig. 16). HNS was not observed on the surface of nanocomposites, see (Fig. 16B and Fig. 16C), even though they moved up to the surface during the phase inversion. This suggests that they have been entrapped within the polymeric matrix close to the top surface. Thus, there would have been no direct contact with the bacterial cells. Both microorganisms were firmly colonized on the surface of unmodified PES membranes, and the surface topography revealed smooth, intact, rod and spherical shaped cells for *E. coli* and *S. aureus*, as shown in (Fig. 16D and Fig. 16F), respectively. However, the nanocomposites greatly influenced the cell wall morphology as confirmed by the markedly damaged and wrinkled surfaces of *E. coli* and *S. aureus* cells, (Fig. 16E and Fig. 16J), respectively. It is worth noting that following the treatment, the bacteria surface turned into rough cells while plentiful cytoplasmic substances were released due to the deterioration to cell membrane. The deformation in the cells membrane and loss of the original bacterium structure may be attributed to Ag^{+} release.

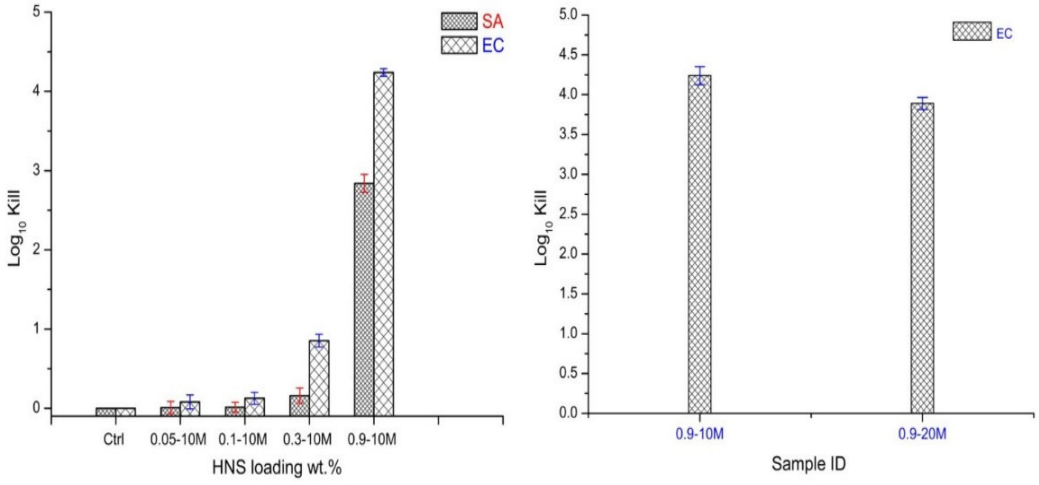

Figure 15: Bacteriocidal activities of nanocomposites agains E. coli and S. aureus (Left), and variation in the antibacterial activity aginst E. coli for nanocomposites prepared using 10HNS and 20HNS (Right).

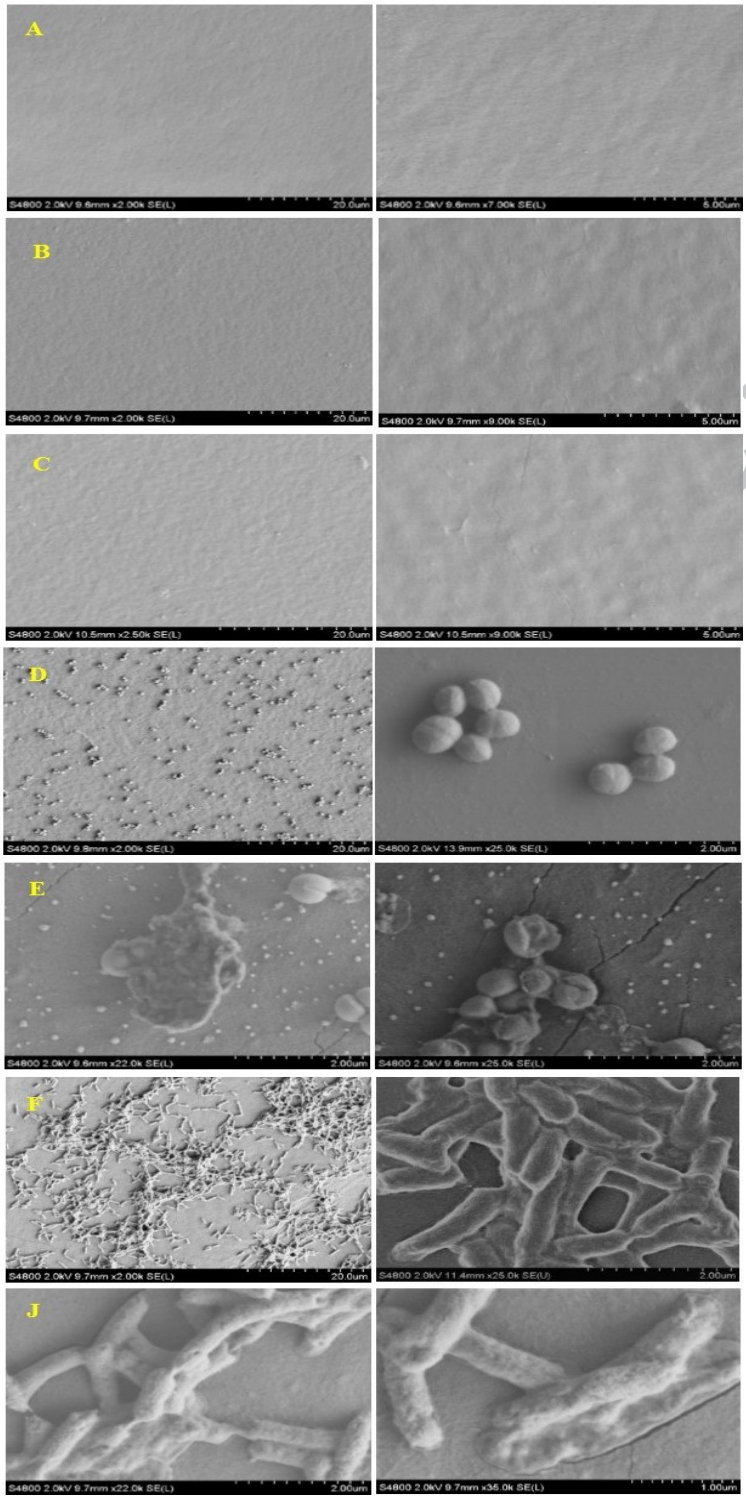

Figure 16: SEM micrographs of (A) virgin control PES membrane, (B) virgin 0.9-10M nanocomposite, (C) Virgin 0.9-20M nanocomposite, (D) control PES membrane fouled with *S. aureus*, (E) 0.9-10M nanocomposite fouled with *S. aureus*, (F) control PES membrane fouled with *E. coli and* (J) 0.9-10M nanocomposite fouled with *E. coli.*

4 Conclusions

This work developed a novel membrane material, based on design and fabrication of a facile, rapid and scalable biocidal HNS for engineered nanocomposite membrane applications, which is effective against both Gram positive and Gram negative bacteria, as confirmed by antibacterial tests using the representative species *E. co.li* and *S. aureus*. Also, characterization techniques have clearly identified the significant influence that Ag/MWCNTs ratio has on the structure and performance of HNS, which in turn impacted on the fabricated nanocomposite membrane structure and process properties to different degrees. Meanwhile, the content of HNS within a PES membrane matrix was found to have little influence on the surface pore size and pore size distribution. However, the addition of the HNS to form a nanocomposite membrane had a significant impact on hydrophilicity measurement, pure water flux, surface zeta potential, and bactericidal performance of the nanocomposites. Moreover, antimicrobial tests suggest Ag^{+} release was the dominant mechanisms against both bacterial species as there was no direct contact between the biocide material and microorganisms. This may be attributed to the fact that the HNS was immobilised within the polymeric chains close to the top surface of the nanocomposites. In conclusion, such biocidal HNS and their incorporation into nanocomposite membranes has great potential in the design of low fouling self-cleaning membranes with a high degree of performance durability and commercial scalability.

Acknowledgment

The authors are grateful for the financial support received from the Higher Committee for Education Development in Iraq (HCED) for providing Ph.D. scholarship to Saif Al Aani.

Nomenclatures	Description
HNS	Hybrid nanostructure
10HNS	Hybrid nanostructure prepared with 10 wt% silver
20HNS	Hybrid nanostructure prepared with 20 wt% silver
MWCNTs	Multiwalled carbon nanotubes
f-MWCNTs	Functionalized multiwalled carbon nanotubes
p-MWNT	Pristine multiwalled carbon nanotubes
AgNPs and nAg	Silver nanoparticles and nanosilver
PES	Polyethersulfone
UF	Ultrafiltration

FTIR	Fourier transmission infrared
XRD	X-ray diffraction
EDX	X-ray energy dispersive spectroscopy
TGA	Thermal gravimetric analysis
SEM	Scanning electron microscope
ZOI	Zone of inhibition
CNTs	Carbone nanotubes
NPs	Nanoparticles
1D-NMs	One-dimensional nanoscale materials
2D-NMs	Two-dimensional nanoscale materials
0D-NPs	Zero-dimensional
NWs	Nanowires
Cu_2O	Copper oxide
TFC	Thin film composite
GO	Graphene oxide
CVD	Chemical vapor diposition
PBS	Phosphate Buffer Solution
MHB	Mueller Hinton Broth
PEG	Polyethylene glycol
PVP	Polyvinylpyrrolidone
HNO_3	Nitric acid
H_2SO_4	Sulphoric acid
HCl	Hydrochloric acid
NMP	N-methyl-2-pyrrolidone
mM	Milimolar
ζ	Zeta potential
CFU	Colony forming unit
PWF	Pure water flux
µp	Mean pore size
σp	Geometric standard deviation
EC	*E. coli*
SA	*S. aureus*

References

[1] H.-C. Flemming, Reverse osmosis membrane biofouling, Experimental Thermal and Fluid Science 14 (1997) 382-391.

[2] A. Subramani, E. Hoek, Direct observation of initial microbial deposition onto reverse osmosis and nanofiltration membranes, Journal of Membrane Science 319 (2008) 111-125.

[3] S. Iravani, H. Korbekandi, S. Mirmohammadi, B. Zolfaghari, Synthesis of silver nanoparticles: chemical, physical and biological methods, Research in pharmaceutical sciences 9 (2014) 385.

[4] M. Ahamed, M.S. Alsalhi, M.K. Siddiqui, Silver nanoparticle applications and human health, Clinica Chimica Acta 411 (2010) 1841-1848.

[5] J.S. Kim, E. Kuk, K.N. Yu, J.H. Kim, S.J. Park, H.J. Lee, S.H. Kim, Y.K. Park, Y.H. Park, C.Y. Hwang, Y.K. Kim, Y.S. Lee, D.H. Jeong, M.H. Cho, Antimicrobial effects of silver nanoparticles, Nanomedicine 3 (2007) 95-101.

[6] S. Al Aani, C.J. Wright, M.A. Atieh, N. Hilal, Engineering nanocomposite membranes: Addressing current challenges and future opportunities, Desalination 401 (2017) 1-15.
[7] A. Mollahosseini, A. Rahimpour, M. Jahamshahi, M. Peyravi, M. Khavarpour, The effect of silver nanoparticle size on performance and antibacteriality of polysulfone ultrafiltration membrane, Desalination 306 (2012) 41-50.
[8] C. Liu, A.F. Faria, J. Ma, M. Elimelech, Mitigation of Biofilm Development on Thin-Film Composite Membranes Functionalized with Zwitterionic Polymers and Silver Nanoparticles, Environ Sci Technol 51 (2017) 182-191.
[9] M.S. Mauter, Y. Wang, K.C. Okemgbo, C.O. Osuji, E.P. Giannelis, M. Elimelech, Antifouling ultrafiltration membranes via post-fabrication grafting of biocidal nanomaterials, ACS Appl Mater Interfaces 3 (2011) 2861-2868.
[10] A.M. Dias, A. Hussain, A.S. Marcos, A.C. Roque, A biotechnological perspective on the application of iron oxide magnetic colloids modified with polysaccharides, Biotechnology Advance 29 (2011) 142-155.
[11] X. Kang, Z. Mai, X. Zou, P. Cai, J. Mo, Glucose biosensors based on platinum nanoparticles-deposited carbon nanotubes in sol-gel chitosan/silica hybrid, Talanta 74 (2008) 879-886.
[12] W. Wang, P. Serp, P. Kalck, C.G. Silva, J.L. Faria, Preparation and characterization of nanostructured MWCNT-TiO2 composite materials for photocatalytic water treatment applications, Materials Research Bulletin 43 (2008) 958-967.
[13] T. Welderfael, M. Pattabi, R.M. Pattabi, A.K.T. G, Photocatalytic activity of Ag-N co-doped ZnO nanorods under visible and solar light irradiations for MB degradation, Journal of Water Process Engineering 14 (2016) 117-123.
[14] Z. Xu, S. Ye, G. Zhang, W. Li, C. Gao, C. Shen, Q. Meng, Antimicrobial polysulfone blended ultrafiltration membranes prepared with Ag/Cu2O hybrid nanowires, Journal of Membrane Science 509 (2016) 83-93.
[15] A.F. Faria, C. Liu, M. Xie, F. Perreault, L.D. Nghiem, J. Ma, M. Elimelech, Thin-film composite forward osmosis membranes functionalized with graphene oxide–silver nanocomposites for biofouling control, Journal of Membrane Science 525 (2017) 146-156.
[16] P. Gunawan, C. Guan, X. Song, Q. Zhang, S.S.J. Leong, C. Tang, Y. Chen, M.B. Chan-Park, M.W. Chang, K. Wang, Hollow fiber membrane decorated with Ag/MWNTs: toward effective water disinfection and biofouling control, ACS nano 5 (2011) 10033-10040.
[17] Y. Chen, Y. Zhang, J. Liu, H. Zhang, K. Wang, Preparation and antibacterial property of polyethersulfone ultrafiltration hybrid membrane containing halloysite nanotubes loaded with copper ions, Chemical Engineering Journal 210 (2012) 298-308.
[18] D. Roy, N. Tiwari, S. Kanojia, K. Mukhopadhyay, A.K. Saxena, Insight into the Mechanism of Decontamination and Disinfection at the Functionalized Carbon Nanotube–Polymer Interfaces, The Journal of Physical Chemistry C 119 (2015) 16678-16687.
[19] Z. Xu, T. Wu, J. Shi, K. Teng, W. Wang, M. Ma, J. Li, X. Qian, C. Li, J. Fan, Photocatalytic antifouling PVDF ultrafiltration membranes based on synergy of graphene oxide and TiO 2 for water treatment, Journal of Membrane Science 520 (2016) 281-293.
[20] K. Balasubramanian, M. Burghard, Chemically functionalized carbon nanotubes, Small 1 (2005) 180-192.
[21] J. Chen, G. Lu, Carbon nanotube-nanoparticle hybrid structures, INTECH Open Access Publisher2010.
[22] G.A. Sotiriou, S.E. Pratsinis, Antibacterial activity of nanosilver ions and particles, Environmental science & technology 44 (2010) 5649-5654.
[23] Y. Hu, C. Guo, Carbon nanotubes and carbon nanotubes/metal oxide heterostructures: synthesis, characterization and electrochemical property, Carbon nanotubes—growth and applications. InTech, Croatia (2011) 3-34.

[24] V. Gomez, A.M. Balu, J.C. Serrano-Ruiz, S. Irusta, D.D. Dionysiou, R. Luque, J. Santamaría, Microwave-assisted mild-temperature preparation of neodymium-doped titania for the improved photodegradation of water contaminants, Applied Catalysis A: General 441-442 (2012) 47-53.
[25] E. Vázquez, M. Prato, Carbon nanotubes and microwaves: interactions, responses, and applications, Acs Nano 3 (2009) 3819-3824.
[26] Y. Lin, D.W. Baggett, J.-W. Kim, E.J. Siochi, J.W. Connell, Instantaneous Formation of Metal and Metal Oxide Nanoparticles on Carbon Nanotubes and Graphene via Solvent-Free Microwave Heating, ACS Applied Materials & Interfaces 3 (2011) 1652-1664.
[27] S. Singh, K. Khulbe, T. Matsuura, P. Ramamurthy, Membrane characterization by solute transport and atomic force microscopy, Journal of Membrane Science 142 (1998) 111-127.
[28] G. Singh, E.M. Joyce, J. Beddow, T.J. Mason, Evaluation of antibacterial activity of ZnO nanoparticles coated sonochemically onto textile fabrics, The Journal of Microbiology, Biotechnology and Food Sciences 2 (2012) 106.
[29] T. Somanathan, K. Prasad, K.K. Ostrikov, A. Saravanan, V.M. Krishna, Graphene oxide synthesis from agro waste, Nanomaterials 5 (2015) 826-834.
[30] R. Yudianti, H. Onggo, Y.S. Sudirman, T. Iwata, J.-i. Azuma, Analysis of functional group sited on multi-wall carbon nanotube surface, Open Materials Science Journal 5 (2011) 242-247.
[31] N. Mkhondo, T. Magadzu, Effects of different acid-treatment on the nanostructure and performance of carbon nanotubes in electrochemical hydrogen storage, Digest Journal of Nanomaterials & Biostructures (DJNB) 9 (2014).
[32] F.C. Moraes, M.F. Cabral, L.H. Mascaro, S.A.S. Machado, The electrochemical effect of acid functionalisation of carbon nanotubes to be used in sensors development, Surface Science 605 (2011) 435-440.
[33] B.-h. Ji, Structural Characterization for Carbon Nanotubes Treated with Concentrated Nitric Acid, Asian Journal of Chemistry 24 (2012) 4271.
[34] F. Alimohammadi, M.P. Gashti, A. Shamei, A. Kiumarsi, Deposition of silver nanoparticles on carbon nanotube by chemical reduction method: Evaluation of surface, thermal and optical properties, Superlattices and Microstructures 52 (2012) 50-62.
[35] W. Yuan, G. Jiang, J. Che, X. Qi, R. Xu, M.W. Chang, Y. Chen, S.Y. Lim, J. Dai, M.B. Chan-Park, Deposition of silver nanoparticles on multiwalled carbon nanotubes grafted with hyperbranched poly (amidoamine) and their antimicrobial effects, The Journal of Physical Chemistry C 112 (2008) 18754-18759.
[36] G. Vuković, A. Marinković, M. Obradović, V. Radmilović, M. Čolić, R. Aleksić, P.S. Uskoković, Synthesis, characterization and cytotoxicity of surface amino-functionalized water-dispersible multi-walled carbon nanotubes, Applied Surface Science 255 (2009) 8067-8075.
[37] C.-M. Chen, M. Chen, F.-C. Leu, S.-Y. Hsu, S.-C. Wang, S.-C. Shi, C.-F. Chen, Purification of multi-walled carbon nanotubes by microwave digestion method, Diamond and Related Materials 13 (2004) 1182-1186.
[38] M. Baro, P. Nayak, T.T. Baby, S. Ramaprabhu, Green approach for the large-scale synthesis of metal/metal oxidenanoparticle decorated multiwalled carbon nanotubes, J. Mater. Chem. A 1 (2013) 482-486.
[39] B.P. Vinayan, R. Nagar, V. Raman, N. Rajalakshmi, K.S. Dhathathreyan, S. Ramaprabhu, Synthesis of graphene-multiwalled carbon nanotubes hybrid nanostructure by strengthened electrostatic interaction and its lithium ion battery application, Journal of Materials Chemistry 22 (2012) 9949.

[40] D.N. Travessa, F.S.d. Silva, F.H. Cristovan, A.M. Jorge Jr, K.R. Cardoso, Ag ion decoration for surface modifications of multi-walled carbon nanotubes, Materials Research 17 (2014) 687-693.
[41] Y. Lin, K.A. Watson, M.J. Fallbach, S. Ghose, J.G. Smith Jr, D.M. Delozier, W. Cao, R.E. Crooks, J.W. Connell, Rapid, solventless, bulk preparation of metal nanoparticle-decorated carbon nanotubes, ACS nano 3 (2009) 871-884.
[42] M. Madigan, J. Martinko, Brock Biology of Microorganisms. 11th EditionPrentice Hall, USA, 2005.
[43] H. Sofiah, A. Nora'aini, M. Marinah, The Influence of Polymer Concentration on Performance and Morphology of Asymmetric Ultrafiltration Membrane for Lysozyme Separation, Journal of Applied Sciences(Faisalabad) 10 (2010) 3325-3330.
[44] A. Rahimpour, M. Jahanshahi, S. Khalili, A. Mollahosseini, A. Zirepour, B. Rajaeian, Novel functionalized carbon nanotubes for improving the surface properties and performance of polyethersulfone (PES) membrane, Desalination 286 (2012) 99-107.
[45] J. Gilron, S. Belfer, P. Väisänen, M. Nyström, Effects of surface modification on antifouling and performance properties of reverse osmosis membranes, Desalination 140 (2001) 167-179.
[46] D. Rana, T. Matsuura, Surface modifications for antifouling membranes, Chemical reviews 110 (2010) 2448-2471.
[47] A. Khalid, A.A. Al-Juhani, O.C. Al-Hamouz, T. Laoui, Z. Khan, M.A. Atieh, Preparation and properties of nanocomposite polysulfone/multi-walled carbon nanotubes membranes for desalination, Desalination 367 (2015) 134-144.
[48] T.E. Thomas, S.A. Aani, D.L. Oatley-Radcliffe, P.M. Williams, N. Hilal, Laser Doppler Electrophoresis and electro-osmotic flow mapping: A novel methodology for the determination of membrane surface zeta potential, Journal of Membrane Science 523 (2017) 524-532.
[49] C. Liu, L. Shi, R. Wang, Enhanced hollow fiber membrane performance via semi-dynamic layer-by-layer polyelectrolyte inner surface deposition for nanofiltration and forward osmosis applications, Reactive and Functional Polymers 86 (2015) 154-160.
[50] M. De Kwaadsteniet, M. Botes, T.E. Cloete, Application of Nanotechnology in Antimicrobial Coatings in the Water Industry, Nano 06 (2011) 395-407.

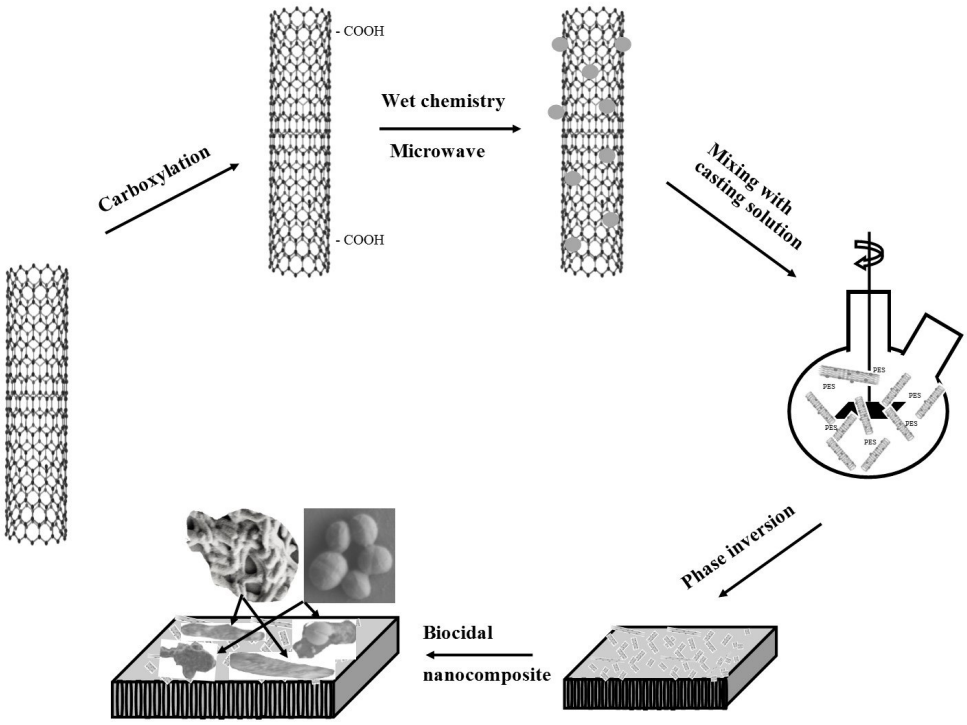

Highlights:

- Novel, rapid and facile method for decorating MWCNTs surface with silver nanoparticles.
- Physical deposition of Ag NPs on MWCNTs via microwave treatment.
- Self-cleaning/antimicrobial nanocomposite membranes for wastewater and desalination applications.
- Long term antibacterial activity for polymeric membranes blended with Ag-MWCNTs.
- Role of Ag-NPs size on the bacteriostatic activity of nanocomposite membranes against E. coli and St. aureus.